TexQ: Zero-shot Network Quantization with Texture Feature Distribution Calibration

Xinrui Chen, Yizhi Wang, Renao Yan*, Yiqin Liu, Tian Guan*, Yonghong He
Tsinghua Shenzhen International Graduate School, Tsinghua University
{cxr22, yz-wang22, yra21, liuyiqin20}@mails.tsinghua.edu.cn
{guantian, heyh}@sz.tsinghua.edu.cn

Abstract

Quantization is an effective way to compress neural networks. By reducing the bit width of the parameters, the processing efficiency of neural network models at edge devices can be notably improved. Most conventional quantization methods utilize real datasets to optimize quantization parameters and fine-tune. Due to the inevitable privacy and security issues of real samples, the existing real-data-driven methods are no longer applicable. Thus, a natural method is to introduce synthetic samples for zero-shot quantization (ZSQ). However, the conventional synthetic samples fail to retain the detailed texture feature distributions, which severely limits the knowledge transfer and performance of the quantized model. In this paper, a novel ZSQ method, TexQ is proposed to address this issue. We first synthesize a calibration image and extract its calibration center for each class with a texture feature energy distribution calibration method. Then, the calibration centers are used to guide the generator to synthesize samples. Finally, the mixup knowledge distillation module is introduced to diversify the synthetic samples for fine-tuning. Extensive experiments on CIFAR10/100 and ImageNet show that TexQ is observed to perform state-of-the-art in low bit width quantization. For example, when ResNet-18 is quantized to 3-bit, TexQ achieves a 12.18% top-1 accuracy increase on ImageNet compared to state-of-the-art methods.

1 Introduction

Limited by the computing capability of edge devices such as mobile phones, deep neural network models inevitably require compression for terminal scenarios [1, 2]. Compared to popular compressing methods such as pruning and distillation, quantization is easier to achieve lightweight and hardware compatibility [3, 4, 5, 6]. By compressing floating-point parameters to low-bit fixed-point integer, quantization reduces the resource footprint and improves computing efficiency. For example, when moving the parameters tensor (weights and activation) from 32 to 4 bits, the memory consumption is reduced by a factor of 8, while the computational overhead of matrix multiplication goes down by a factor of 64 at a squared rate. Most research on quantization focuses on quantization-aware training (QAT) [7, 8, 9, 10] and post-training quantization (PTQ) [11, 12, 13, 14, 15, 16]. QAT introduces fake quantization nodes when training and achieves performance close to full precision. However, it relies on the full training set and lacks a uniform specification, making it unfriendly to deploy. Thus, PTQ has gained attention, which only requires a small part of the training set to statistically optimize the quantization parameters [17, 18, 19, 20].

Due to privacy and security constraints, access to certain real data might be prohibited [21], such as patient medical images, confidential business information, etc. Therefore, zero-shot quantization

[*] Corresponding author

37th Conference on Neural Information Processing Systems (NeurIPS 2023).

(ZSQ) [22, 23, 21, 24, 25] is proposed to circumvent this limitations. Among previous studies, synthetic sample-based methods [21, 24, 25] have attracted attention by their excellent performance. Most studies synthesize samples that resemble the distribution of the real samples by extracting statistics in the full precision model, such as batch-normalization statistics [21], categorical labels [24], intermediate features [25], etc. However, despite a good fit to the model statistics and high classification confidence, there is still a huge gap between the texture feature distribution they contain and that of real samples. Such a phenomenon is likely to result in bad performance, as studies show that CNNs rely on texture feature to make decisions, for texture feature is "easy to learn" for CNNs [26, 27, 28]. In addition, the conventional multiple-constraint paradigm limits the diversity of synthetic samples [29, 30].

To tackle the above problems, the following exploratory experiments were carried out. Firstly, local binary pattern (LBP) [32] was introduced to characterize the texture feature. A batch of real samples and conventional synthetic samples with class confidence above 99.9% were extracted their LBP feature for clustering. As presented in Figure 1, the domain gap (point distribution) and diversity gap (point density) can be observed. We further explored the texture bias of the quantized model to prove the importance of texture feature. As shown in Figure 2, same model was respectively quantized with real samples and conventional synthetic samples, and tested in four image patterns: original, greyscale (removes color feature), binary (removes color and texture feature), and edge (retains shape feature and restores a few texture feature). It illustrates that removing texture feature causes a sharp performance decrease. The model quantized with synthetic samples drops off a lot on performance while restoring some of the texture feature in Figure 2d can recover its performance. These experiments imply that the ZSQ model is strongly biased towards texture feature and tends to make decisions with it. Inspired by the experiments, an intuitive idea is to calibrate the synthetic samples to retain the texture feature distribution, which facilitates the model to learn and improve its performance.

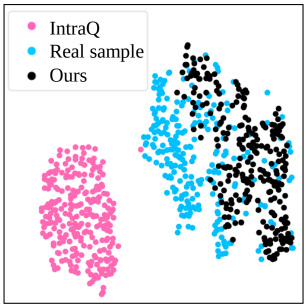

Figure 1: LBP feature clustering of samples from CIFAR10, IntraQ and our method. Visualization with t-SNE [31]

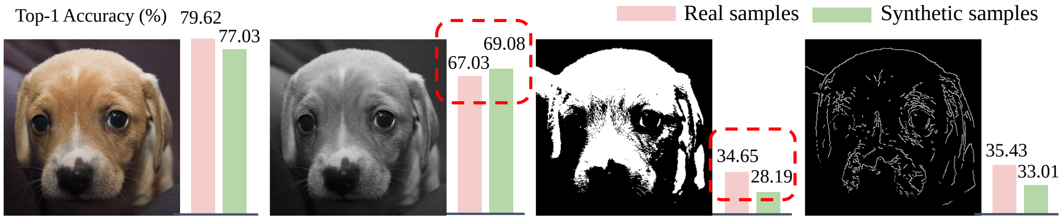

(a) Original (b) Greyscale (c) Binary (d) Edge

Figure 2: Test results of real/synthetic samples quantized model on CIFAR10 in 4 image patterns.

In this work, we propose TexQ, a zero-shot quantization method using synthetic calibration centers to calibrate samples and retain texture feature distributions. We first generate a calibration images and its center for each class. Further, the centers guide the generator to synthesize samples. The two-stage synthetic sample paradigm alleviates the homogeneity caused by multiple constraints. Finally, mixup knowledge distillation is introduced to enhance sample diversity and avoid overfitting. With the above methods, the proposed TexQ performs state-of-the-art on various datasets and model settings.

2 Related work

2.1 Texture feature extraction

Texture feature is powerful visual cue that provides useful information in identifying objects or regions of interest in images [33]. To make use of these cues, texture feature extraction methods has been widely used in natural image processing, among which filtering approaches are proven to be successful, including LAWS filters, dyadic Gabor filter banks, wavelet transforms and so on [34]. Studies [35, 36, 37] have shown that image texture feature are conductive to image classification and are class separable. For instance, [38] introduce GLCM and Gabor texture feature from regions of interest for better mammogram classification. Recently, many studies [39, 40, 41] identify the importance of textures feature for CNNs. [39] found that texture representations could capture the statistical characteristics of images for CNNs. [40] showed that classic CNNs were unable to recognize sketches where textures are missing and shapes are left. Similarly, [41, 42] validated that CNNs were biased towards textures than shapes, for example, ResNet-50 biased 77.9% texture.

2.2 Zero-shot quantization

Most zero-shot quantization (also called data-free quantization) studies try to recover the quantization error from three perspectives. The first perspective designs quantization parameters by using model properties [22, 23, 43, 44] without acquiring any data. For instance, Nagel et al. [22] proposed a scale-equivariance property of activation functions to equalize the weight ranges of the network. Meller et al. [44] highlighted an inversely proportional factorization of convolutional neural networks to decrease the degradation caused by quantization. The above methods avoid the access to data but suffer from severe performance degradation in low bit widths. For example, DFQ achieved a 0.11% top-1 accuracy in the 4-bit MobileNetV2 case [22, 24]. Therefore, more ZSQ methods resort to synthetic samples. The second perspective adopts optimization-based methods to synthesize samples by aligning the statistics in the full-precision network [21, 30, 29]. ZeroQ [21] adopted batch normalization statistics alignment to optimize the standard Gaussian noise. DSG [30] proposed a slack distribution alignment to diversify samples. IntraQ [29] highlighted the intra-class heterogeneity and retained this property in the synthetic samples for better performance. The third perspective adopts a generator to synthesize samples [24, 45, 46, 47, 48]. For example, GDFQ [24] proposed a knowledge-matching generator to produce synthetic data with labels by introducing the cross-entropy loss. ClusterQ [45] utilized the feature distribution alignment to imitate the distribution of real data. AdaDFQ [47] proposed a zero-sum game to adaptively regulate the adaptability of synthetic samples. The existing studies provide us effective method to fit statistics in full-precision models, however, none of these considered texture feature distribution in synthetic samples, though it is fundamental for CNNs to learn and make decisions. To the extent of our knowledge, this work is the first to consider texture feature in ZSQ, introducing a synthetic calibration center to calibrate synthetic samples.

3 Methodology

3.1 Preliminaries

3.1.1 Quantizer

Following ZeroQ [21], asymmetric quantization is adopted. Given a floating-point value x_f (weights or activations) and quantization bit width BW, the quantized integer x_q can be obtained as:

$$x_q = Clip(\lfloor x_f \cdot S - ZP \rceil, 0, 2^{BW} - 1) \tag{1}$$

where $S = \frac{2^{BW}-1}{x_{f\,\max} - x_{f\,\min}}$ is the scaling factor mapping the floating-point number to a fixed-point integer, $ZP = x_{f\,\min} \cdot S$ is the zero point mapping the floating-point minimum to zero, $\lfloor \mathit{input} \rceil$ rounds its input to the nearest integer. $Clip(tensor, r_{min}, r_{max})$ clamps the tensor elements to be between r_{min} and r_{max}. The dequantized value x_d can be obtained as:

$$x_d = \frac{x_q + ZP}{S}. \tag{2}$$

3.1.2 Data synthesis

PTQ requires a small real dataset $D = \{(x,\ y)\}$ containing samples x and labels y. Similarly, most ZSQ introduce synthetic sample sets $\overline{D} = \{(\overline{x},\ \overline{y})\}$. To fit the batch normalization statistics (BNS) in the full-precision model (F), a basic principle [21, 45, 29] is using BNS alignment loss in Eq. 3.

$$\mathcal{L}_{BNS} = \sum_{l=1}^{L} \left\| \mu_l(\overline{x}) - {\mu_l}^F \right\|_2 + \left\| \sigma_l(\overline{x}) - {\sigma_l}^F \right\|_2, \tag{3}$$

where ${\mu_l}^F$ and ${\sigma_l}^F$ are the running mean and variance stored in the l-th BN layer of F. The mean and variance of the synthetic sample batch $\overline{x}$ in the l-th layer of F are given by $\mu_l(\overline{x})$ and $\sigma_l(\overline{x})$.

Given generator G, standard Gaussian noise z, and a target label $\overline{y}$, the synthetic sample can be obtained as $\overline{x} = G\left(z|\overline{y}\right)$. The cross-entropy loss in Eq. 4 is used to generate label-oriented samples [24, 19].

$$\mathcal{L}_{CE} = \mathbb{E}_{(x,y)\sim\{(\bar{x},\bar{y})\}} \left[Cross\text{-}entropy\left(F(\bar{x}), \bar{y}\right)\right]. \tag{4}$$

3.2 Texture feature distribution calibration

In this section, the calibration method and mixup knowledge distillation module are proposed. The framework of our TexQ is illustrated in Figure 3.

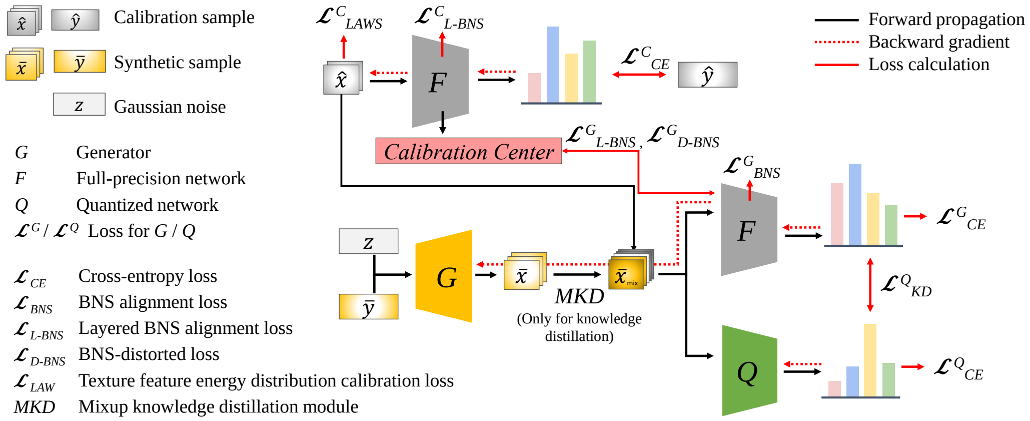

$\hat{x}$ $\hat{y}$ Calibration sample
$\bar{x}$ $\bar{y}$ Synthetic sample
z Gaussian noise
G Generator
F Full-precision network
Q Quantized network
$\mathcal{L}^G$ / $\mathcal{L}^Q$ Loss for G / Q
$\mathcal{L}_{CE}$ Cross-entropy loss
$\mathcal{L}_{BNS}$ BNS alignment loss
$\mathcal{L}_{L\text{-}BNS}$ Layered BNS alignment loss
$\mathcal{L}_{D\text{-}BNS}$ BNS-distorted loss
$\mathcal{L}_{LAW}$ Texture feature energy distribution calibration loss
MKD Mixup knowledge distillation module
$\mathcal{L}^C_{LAWS}$
$\mathcal{L}^C_{L\text{-}BNS}$
$\mathcal{L}^C_{CE}$
Forward propagation
Backward gradient
Loss calculation
Calibration Center
$\mathcal{L}^G_{L\text{-}BNS}$, $\mathcal{L}^G_{D\text{-}BNS}$
$\mathcal{L}^G_{BNS}$
$\mathcal{L}^G_{CE}$
$\mathcal{L}^Q_{KD}$
$\mathcal{L}^Q_{CE}$
$\bar{x}_{mix}$
MKD
(Only for knowledge distillation)

Figure 3: An overview of the proposed framework TexQ. Calibration centers are produced to guide G to synthesize samples. Q is fine-tuned with both calibration samples and synthetic samples.

3.2.1 Texture feature energy distribution calibration loss

To quantitatively measure the texture feature distribution, LAWS texture feature energy [49, 50] is introduced. We select four 1-dimensional filters provided by LAWS: E$_5$=[-1, -2, 0, 2, 1], S$_5$=[-1, 0, 2, 0, -1], W$_5$=[-1, 2, 0, -2, 1], R$_5$=[1, -4, 6, -4, 1], which stand for edge, spot, wave, and ripple. By convolving two 1-dimensional LAWS filters of size 1×5 with each other, a total of 16 2-dimensional filters of size 5×5 can be obtained. Each filter extracts a basic element of the texture, for example, R$_5$R$_5$ denotes a high-frequency point filter, and E$_5$S$_5$ denotes a V shape filter. To be specific, the calculation procedure of R$_5$R$_5$ is given as an example in Eq. 5.

$$R_5R_5 = {R_5}^T * R_5 = \begin{bmatrix} 1 \\ -4 \\ 6 \\ -4 \\ 1 \end{bmatrix} * \begin{bmatrix} 1 & -4 & 6 & -4 & 1 \end{bmatrix} = \begin{bmatrix} 1 & -4 & 6 & -4 & 1 \\ -4 & 16 & -24 & 16 & -4 \\ 6 & -24 & 36 & -24 & 6 \\ -4 & 16 & -24 & 16 & -4 \\ 1 & -4 & 6 & -4 & 1 \end{bmatrix} \tag{5}$$

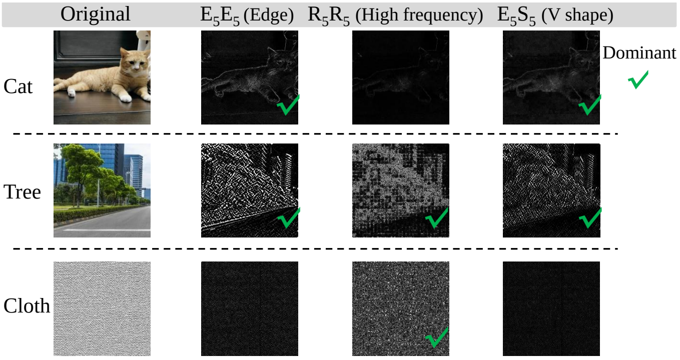

Figure 4: Features extracted with LAWS filters.

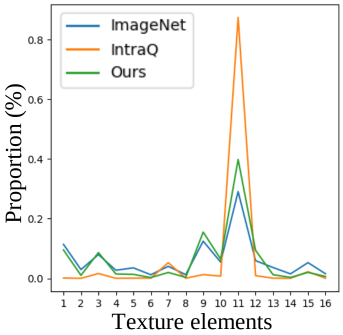

Figure 5: Visualization of distribution T from different samples.

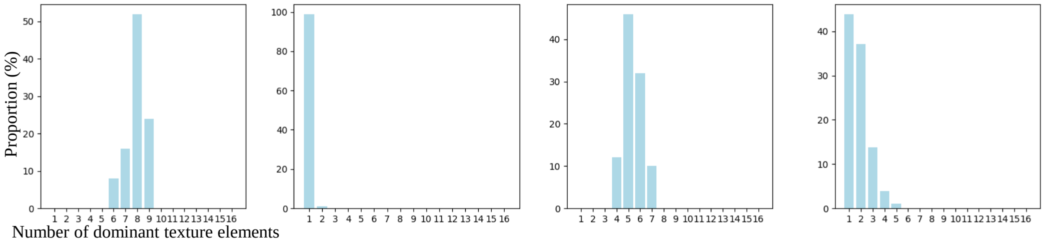

(a) ImageNet (b) Synthetic sample (IntraQ) (c) Calibration sample (Ours) (d) Synthetic sample (Ours)

Figure 6: Dominant texture elements number distribution of samples from the ImageNet training set, IntraQ synthetic samples, calibration images as well as synthetic samples generated by our method. Synthetic samples were obtained with pre-trained ResNet-18.

Straightforward visualization of the texture feature extracted by LAWS texture feature filters is provided in Figure 4. It can be observed that different types of images contain different dominant texture feature. For example, the trees with lots of leaves including V-shape, high-frequency points and edge features, and the cat lying on the chair including mainly V-shape and edge features.

It is reasonable to evaluate texture distributions by analyzing basic elements, for complex texture feature are composed of simple elements. We apply 16 filters to obtain the texture feature energy distributions T of a sample as shown in Figure 5. Assuming that the top-k elements in T account for more than 80% are the dominant texture elements, the set of these k elements is recorded as K. As displayed in Figure 6, the real samples (Figure 6a) have at most 9 dominant texture elements, i.e., k $\leq$ 9, while there is almost only 1 in the conventional synthetic samples (Figure 6b). To be detailed, in Figure 5, the distribution curve of the conventional synthetic sample presents a clear peak, indicating a single dominant element, which reduces the intra-class heterogeneity and the information contained. Unlike this, the curve of the real sample presents a detailed texture distribution. To retain this property, texture feature energy distribution calibration loss of Eq. 6 is proposed to dynamically adjust the detailed texture feature distribution of calibration images for each class.

$$\mathcal{L}^{C}{}_{LAWS} = \max\left(\|K_{\max} - \theta_U\|_2 - \varepsilon,\ 0\right) + \max\left(\|(1 - K_{\max}) - \theta_L\|_2 - \varepsilon,\ 0\right), \tag{6}$$

where $K_{\max}$ is the largest element in K. The hyperparameters θ_U, θ_L, and ε control the upper and lower bounds of the elements in K. Specifically, θ_U is the upper bound of $K_{\max}$, and θ_L is the lower bound of the sum of all elements in K except $K_{\max}$. ε is the softness factor to alleviate convergence problem. Both upper and lower bounds are used together to extract detailed distribution.

To introduce the calibration loss, a possible scheme is directly applying constraint to the generator. However, multiple constraints to generator results in slow iterations and homogeneous samples. We adopt a two-stage method, which includes an optimization method to synthesize accurate calibration centers for each class and a generation method to synthesize samples with the constraint on calibration centers.

3.2.2 Layered BNS alignment constraint

Considering that neural networks extract class-independent low-level features (e.g., texture and contours) in shallow layers and class-related high-level features in deep layers, the layered BNS alignment loss ($\mathcal{L}_{L\text{-}BNS}$) is proposed. We adopt loose constraints in shallow layers to facilitate the expression of texture feature and tightened constraints in deep layers to fit class-related information.

In calibration set generation stage, given the calibration set $C = \{(\widehat{x},\ \widehat{y})\}$, the $\mathcal{L}^C{}_{L\text{-}BNS}$ of Eq. 7 constraints C to align the BNS in F.

$$\begin{gathered}\mathcal{L}^C{}_{L\text{-}BNS} = \sum_{l=1}^{L} \left\| w_l \cdot (\mu_l(\widehat{x_c}) - \mu_l{}^F) \right\|_2 + \left\| w_l \cdot \left(\sigma_l(\widehat{x_c}) - \sigma_l{}^F\right) \right\|_2, \\ w_l = \begin{cases} 0.2, 1 \le l < \lceil \frac{L}{2} \rceil - 2 \\ 1.1, \lceil \frac{L}{2} \rceil - 2 \le l \le L \end{cases},\end{gathered} \tag{7}$$

where L is the number of BN layers, $\mu_l(\widehat{x_c})$ and $\sigma_l(\widehat{x_c})$ denote the mean and variance of C in the l-th layer of F. w_l is the loss weight for the l-th layer. $\lceil input \rceil$ returns the smallest integer greater than its input.

In synthetic sample generation stage, $\mathcal{L}^G{}_{L\text{-}BNS}$ in Eq. 8 constrains the generator to synthesize samples that fit the calibration centers of corresponding class label k.

$$\begin{aligned}\mathcal{L}^G{}_{L\text{-}BNS} = & \sum_{l=1}^{L} \left\| w_l \cdot \left[\mu_l\left(\overline{x} | \overline{y} = k\right) - \mu_l{}^C\left(\widehat{x_c} | \widehat{y_c} = k\right)\right] \right\|_2 \\ & + \left\| w_l \cdot \left[\sigma_l\left(\overline{x} | \overline{y} = k\right) - \sigma_l{}^C\left(\widehat{x_c} | \widehat{y_c} = k\right)\right] \right\|_2, w_l = \begin{cases} 0, 1 \le l < \lceil \frac{L}{2} \rceil - 2 \\ 1, \lceil \frac{L}{2} \rceil - 2 \le l \le L \end{cases},\end{aligned} \tag{8}$$

where $\mu_l\left(\overline{x} | \overline{y} = k\right)$ and $\sigma_l\left(\overline{x} | \overline{y} = k\right)$ denote the mean and variance of the synthetic samples. $\mu_l{}^C\left(\widehat{x_c} | \widehat{y_c} = k\right)$ and $\sigma_l{}^C\left(\widehat{x_c} | \widehat{y_c} = k\right)$ are the corresponding mean and variance calibration center.

3.2.3 Mixup knowledge distillation module

Knowledge distillation is commonly used to transfer the output distribution from full-precision model F to the quantized model Q in the fine-tuning stage, which requires diversified samples. Some studies introduce Mixup [51, 48] augmentation to generate samples with mixed labels to fine-tune the quantized model with cross-entropy loss. However, the labels produced by the such methods are not accurate enough, and taking such mixed labels to fine-tune the quantized model tends to be disastrously misleading. Therefore, we advocate discarding mixed labels and taking only mixed samples to knowledge distillate the quantized model, and name this method mixup knowledge distillation. Specifically, as presented in Eq. 9, new sample $\overline{x}_{mix}$ is generated by weighted fusion of 2 samples $\overline{x}_i$ and $\overline{x}_j$ randomly selected in a batch for distillation. Mixup proportion λ is sampled from a standard uniform distribution. The probability p = 20% is observed to perform best.

$$\overline{x}_{mix} = \begin{cases} \lambda \overline{x}_i + (1 - \lambda)\overline{x}_j,\ with\, probability\ p \\ \overline{x}_i,\ with\, probability\ 1 - p \end{cases}, \lambda \sim \mathrm{U}\,(0,\ 1) \tag{9}$$

3.3 Quantization process

3.3.1 Step1: Calibration set generation

In this stage, the calibration set with Gaussian noise initialization is optimized with the loss in Eq. 10, capturing the preferred texture of each class from F. We fix F and back-propagate the loss to the calibration images. For each class, the calibration image is trained for at most 1500 iterations individually, with a warm-up of 150 iterations at half learning rate without $\mathcal{L}^C{}_{LAWS}$. Their BNS are extracted as the calibration centers to guide the generator in the next step.

$$\mathcal{L}^C = \mathcal{L}^C{}_{LAWS} + \alpha_1 \cdot \mathcal{L}^C{}_{L\text{-}BNS} + \alpha_2 \cdot \mathcal{L}^C{}_{CE} \tag{10}$$

3.3.2 Step2: Synthetic samples generation

In this stage, generator G synthesize samples of different classes that fit corresponding calibration centers via ${\mathcal{L}^G}_{L\text{-}BNS}$. Following FDDA [19], BNS-distorted loss in Eq. 11 is introduced to avoid overfitting by Gaussian noise interfering with the calibration center. ν_μ = 0.5 and ν_σ = 1.0 control the distortion degree of mean and variance.

$$\begin{aligned} {\mathcal{L}^G}_{D\text{-}BNS} &= \sum_{l=1}^{L} \left\| w_l \cdot \left[\mu_l \left(\overline{x} | \overline{y} = k \right) - \mathcal{N} \left({\mu_l}^C \left(\widehat{x_c} | \widehat{y_c} = k \right), \nu_\mu \right) \right] \right\|_2 \\ &+ \left\| w_l \cdot \left[\sigma_l \left(\overline{x} | \overline{y} = k \right) - \mathcal{N} \left({\sigma_l}^C \left(\widehat{x_c} | \widehat{y_c} = k \right), \nu_\sigma \right) \right] \right\|_2, w_l = \left\{ \begin{array}{l} 0, 1 \le l < \left\lceil \frac{L}{2} \right\rceil - 2 \\ 1, \left\lceil \frac{L}{2} \right\rceil - 2 \le l \le L \end{array} \right. . \end{aligned} \tag{11}$$

In addition, ${\mathcal{L}^G}_{CE}$ and ${\mathcal{L}^G}_{BNS}$ are used to align the label and BNS of F. Up to this point, the total loss employed by generator G can be summarized in Eq. 12.

$$\mathcal{L}^G = {\mathcal{L}^G}_{CE} + \alpha_3 \cdot {\mathcal{L}^G}_{BNS} + \alpha_4 \cdot {\mathcal{L}^G}_{L\text{-}BNS} + \alpha_5 \cdot {\mathcal{L}^G}_{D\text{-}BNS}. \tag{12}$$

3.3.3 Step3: Quantized model fine-tuning

To make full use of the data, we take both samples in $\overline{D}$ and C as the input of Q and apply cross-entropy loss ${\mathcal{L}^Q}_{CE}$ to fine-tune. Subsequently, both samples in $\overline{D}$ and C are input into the mixup knowledge distillation module to produce mixup samples. With the input of mixup samples, Kullback-Leibler loss in Eq. 13 is applied to transfer the output of F to Q.

$${\mathcal{L}^Q}_{KD} = \mathbb{E}_{(x,y) \sim \mathrm{C} \cup \overline{\mathrm{D}}} \left[Kullback\text{-}Leibler \left(Q(\overline{x}_{mix}), F(\overline{x}_{mix}) \right) \right]. \tag{13}$$

At this point, the overall loss for fine-tuning Q can be summarized as:

$$\mathcal{L}^Q = {\mathcal{L}^Q}_{CE} + \alpha_6 \cdot {\mathcal{L}^Q}_{KD} \tag{14}$$

4 Experiment

4.1 Experimental settings and details

We report top-1 accuracy on validation sets of CIFAR-10/100 [52] and ImageNet [53]. Networks selected include ResNet-20 [54] for CIFAR-10/100, ResNet-18, MobileNetV2 [55] and ResNet-50 for ImageNet. All experiments are implemented with Pytorch [56] via the code of FDDA [19] and IntraQ [29], and run on an NVIDIA GeForce RTX 3090 GPU. Calibration images are iterated with a constant learning rate of 0.05. Generator is imported from GDFQ [24] with a initial learning rate of 1e-3 multiplied by 0.1 every 100 epochs. In fine-tuning, batchsize is 128 for CIFAR-10/100 and 16 for ImageNet, adjusting by cosine annealing [57]. We warm up G for 50 epochs, then update G and Q for 450 epochs. The optimal configurations on trade-off parameters from α_1 to α_6 obtained by grid search are 2, 10, 0.4, 0.02, 1.8, and 20.

4.2 Performance comparison

To demonstrate the efficacy of our TexQ, we conduct experiment in 3/4-bit case, since high accuracy can be easily achieved with a larger bit width. For instance, the advanced AdaDFQ [47] trails full precision with a 0.08% top-1 accuracy in 5-bit ResNet-20 case. In this section, WBAB indicates the weights and activations are quantized to B-bit. Best results in boldface.

4.2.1 CIFAR-10/100

We compare the performance against the advanced ZSQ methods on CIFAR-10/100. As presented in Table 1, our TexQ is observed to achieve state-of-the-art among the competitors, improving the top-1 accuracy by 3.13%/1.58% in 3-bit CIFAR-10/100 case compared to the advanced AdaDFQ. Similar results can be observed in the 4-bit case. In particular, the top-1 accuracy of our TexQ exceeds that of the same framework with real data in 4-bit case, demonstrating that the proposed TexQ can fully extract the feature distribution in simple datasets.

Table 1: Results of ResNet-20 on CIFAR-10/100.

Bit width	Method	Top-1 Accuracy(%)	
		CIFAR-10	CIFAR-100
	Full-precision	93.89	70.33
W4A4	Real data	91.52	66.80
	GDFQ [24] (ECCV 2020)	90.11	63.75
	ARC [58] (IJCAI 2021)	88.55	62.76
	Qimera [48] (NeurIPS 2021)	91.26	65.10
	IntraQ [29] (CVPR 2022)	91.49	64.98
	ARC+AIT [59] (CVPR 2022)	90.49	61.05
	AdaSG [46] (AAAI 2023)	92.10	66.42
	AdaDFQ [47] (CVPR 2023)	92.31	66.81
	TexQ (Ours)	**92.68**	**67.18**
W3A3	GDFQ [24, 47] (ECCV 2020)	75.11	47.61
	ARC [58] (IJCAI 2021)	-	40.15
	Qimera [48, 47] (NeurIPS 2021)	74.43	46.13
	IntraQ [29] (CVPR 2022)	77.07	48.25
	ARC+AIT [59] (CVPR 2022)	-	41.34
	AdaSG [46] (AAAI 2023)	84.14	52.76
	AdaDFQ [47] (CVPR 2023)	84.89	52.74
	TexQ (Ours)	**86.47**	**55.87**

4.2.2 ImageNet

We further compare with competitors on challenging ImageNet, the results are presented in Table 2.

Table 2: Results of ResNet-18, MobileNetV2 and ResNet-50 on ImageNet.

Bit width	Method	Top-1 Accuracy(%)		
		ResNet-18	MobileNetV2	ResNet-50
	Full-precision	71.47	72.49	77.73
W4A4	GDFQ [24] (ECCV 2020)	60.60	59.43	54.16
	ZAQ [25] (CVPR 2021)	52.64	0.10	53.02
	ARC [58] (IJCAI 2021)	61.32	60.13	64.37
	Qimera [48] (NeurIPS 2021)	63.84	61.62	66.25
	IntraQ [29] (CVPR 2022)	66.47	65.10	-
	ARC+AIT [59] (CVPR 2022)	65.73	66.47	68.27
	AdaSG [46] (AAAI 2023)	66.50	65.15	68.58
	AdaDFQ [47] (CVPR 2023)	66.53	65.41	68.38
	TexQ (Ours)	**67.73**	**67.07**	**70.72**
W3A3	GDFQ [24, 47] (ECCV 2020)	20.23	1.46	0.31
	ARC [58] (IJCAI 2021)	23.37	14.30	1.63
	Qimera [48, 47] (NeurIPS 2021)	1.17	-	-
	AdaSG [46] (AAAI 2023)	37.04	26.90	16.98
	AdaDFQ [47] (CVPR 2023)	38.10	28.99	17.63
	TexQ (Ours)	**50.28**	**32.80**	**25.27**

Bit width For low bit width case, conventional ZSQ methods suffer from a huge accuracy loss, while our TexQ performs good generalization capability. Specifically, for 4-bit ResNet-18 case, TexQ achieving 67.73% accuracy, outperforming AdaDFQ by 1.2%. In 3-bit case, TexQ reaches 50.28% outstanding accuracy, outperforming AdaDFQ by 12.18%, with a standard deviation of 0.34 in 5 repeated experiments. Similar results were obtained in MobileNetV2.

Network Size Larger models are likely lead to poor performance with existing ZSQ methods, especially in low bit width case. For example, in 3-bit case, Qimera [48, 47] performs well on the small ResNet-20, while achieves only 1.17% accuracy on the larger ResNet-18. In contrast, our TexQ achieved 55.87% ultra-low when quantizing ResNet-18 to 3-bit, and leads AdaDFQ with 7.64% on 3-bit ResNet50 case. These results again demonstrate the effectiveness of our method.

4.3 Ablation study

Hyperparameters After empirical initialization, the hyperparameters k, θ_U, θ_L, and ε are searched for their optimal value with grid search by quantizing ResNet-18 to 3-bit on ImageNet, as displayed in Figure 7. The optimal configurations are k=9, θ_U=0.3, θ_L=0.5, and ε=0.015. The hyperparameter k represents the number of dominant texture elements, whose optimal value of k=9 is consistent with what we observe in the real samples. The sum of the optimal values of θ_U and θ_L is 0.8, which fits our assumptions about the proportion of dominant texture elements. To avoid complex searches, these parameters were used for all experiments. While this may not be optimal for all networks, it is sufficient to exhibit the advanced performance of TexQ.

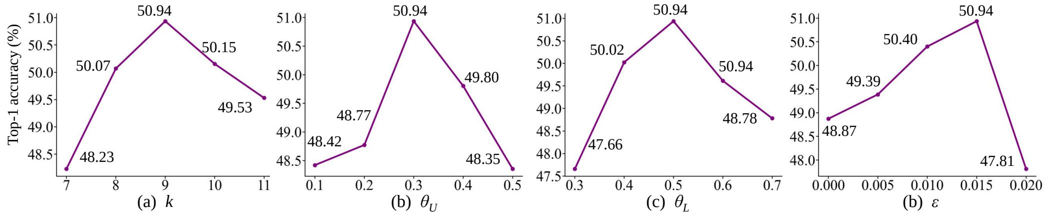

(a) k (b) θ_U (c) θ_L (b) ε

Figure 7: Influence of the hyperparameters.

Modules Ablation on key modules including $\mathcal{L}^C{}_{LAWS}$ (Eq. 6), $\mathcal{L}^C{}_{L\text{-}BNS}$ (Eq. 7) and mixup knowledge distillation (MKD, Eq. 9) is conducted. As presented in Table 3, dropping one or two of them results in an accuracy loss. The largest accuracy loss (8.37%) is observed when both $\mathcal{L}^C{}_{LAWS}$ and $\mathcal{L}^C{}_{L\text{-}BNS}$ are removed, which indicates their cooperative relationship: $\mathcal{L}^C{}_{L\text{-}BNS}$ loosens the shallow layers constraint, facilitating $\mathcal{L}^C{}_{LAWS}$ to calibrate.

Table 3: Ablations on modules. We report the top-1 accuracy of 3-bit ResNet-18 on ImageNet.

$\mathcal{L}^C{}_{LAWS}$	$\mathcal{L}^C{}_{L\text{-}BNS}$	MKD	Top-1 Accuracy(%)
✓	✓	✓	**50.94**
✓	✓		49.03
✓		✓	43.31
	✓	✓	49.63
✓			42.65
	✓		49.00
		✓	42.57

5 Discussion

5.1 Why does TexQ work?

Mitigating the domain gap Our synthetic samples with calibration match the real distribution better, as presented in Figure 1 and Figure 6. Further, Figure 5 shows our synthetic sample has a more detailed texture distribution similar to the real one.

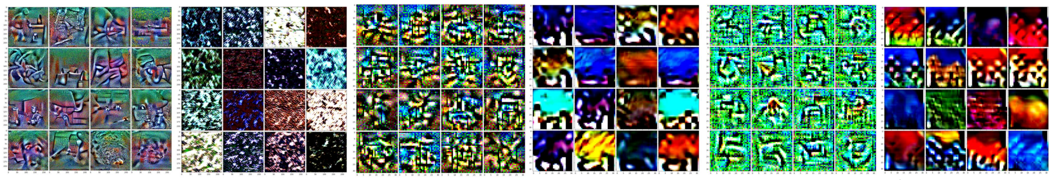

(a) ImageNet (IntraQ) (b) ImageNet (Ours) (c) CIFAR10 (IntraQ) (d) CIFAR10 (Ours) (e) CIFAR100 (IntraQ) (f) CIFAR100 (Ours)

Figure 8: Visualization of synthetic samples. For ImageNet and CIFAR10/100, samples are obtained with ResNet-18 and ResNet-20, respectively. The advanced IntraQ was selected as a competitor.

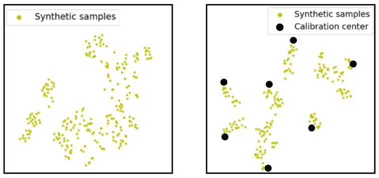

(a) Without Calibration (b) Introduce Calibration

Figure 9: Visualization of the running mean of BNS in ResNet-20.

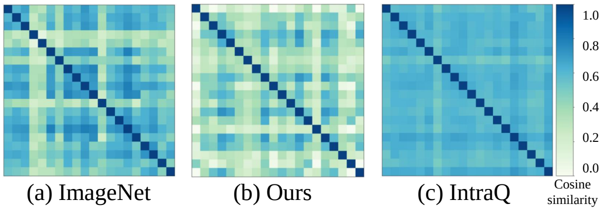

(a) ImageNet (b) Ours (c) IntraQ

Figure 10: Cosine similarity confusion matrix of samples. Synthetic samples are obtained with ResNet-18.

Increasing inter-class distance As displayed in Figure 9a, the class centers of samples from conventional methods is unclear, limiting the inter-class distance. The situation is improved by introducing calibration centers, as shown in Figure 9b.

Enhancing sample diversity Figure 1 shows our synthetic samples scatter a lot compared with IntraQ, implying the enhancement of sample diversity. To put it bluntly, synthetic images from different methods are visualized in Figure 8, showing the improvement in color and texture diversity of our samples. Further, the intra-class diversity is observed through cosine similarity confusion matrix of samples in Figure 10, showing that our samples reach a similar diversity to the real ones.

5.2 Limitations and future work

This work is built upon the concept of "texture", and the texture filters adopted are designed manually. Thus, the application to other tasks with different modality would be limited. We envision adding training process to the filters, which would generalize the calibration method proposed to other modality. Low-bit quantization remains a challenge. For instance, TexQ achieve 70.72% accuracy by quantizing ResNet-50 to 4-bit, while it drops to 25.27% in 3-bit case. The introduction of advanced distillation methods holds promise for more better results.

6 Conclusion

In this paper, we observe a non-negligible detailed texture distribution in the real samples. To retain this property in synthetic samples, we introduce synthetic calibration images and centers to calibrate the generator. To diversify the samples, mixup knowledge distillation module is introduce to create diversified samples for fine-tuning. Extensive experiments show our state-of-the-art performance on mainstream networks and datasets, especially for low bit width quantization.

Acknowledgment

This work was supported by the Science and Technology Research Program of Shenzhen City (No. KCXFZ20201221173207022, No.WDZC20200821141349001) and the Jilin Fuyuan Guan Food Group Co., Ltd.

References

[1] Benoit Jacob, Skirmantas Kligys, Bo Chen, Menglong Zhu, Matthew Tang, Andrew Howard, Hartwig Adam, and Dmitry Kalenichenko. Quantization and training of neural networks for efficient integer-arithmetic-only inference. In *Proceedings of the IEEE conference on computer vision and pattern recognition*, pages 2704–2713, 2018.

[2] Song Han, Xingyu Liu, Huizi Mao, Jing Pu, Ardavan Pedram, Mark A Horowitz, and William J Dally. Eie: Efficient inference engine on compressed deep neural network. *ACM SIGARCH Computer Architecture News*, 44(3):243–254, 2016.

[3] Yu-Hsin Chen, Tien-Ju Yang, Joel Emer, and Vivienne Sze. Eyeriss v2: A flexible accelerator for emerging deep neural networks on mobile devices. *IEEE Journal on Emerging and Selected Topics in Circuits and Systems*, 9(2):292–308, 2019.

[4] Lei Deng, Guoqi Li, Song Han, Luping Shi, and Yuan Xie. Model compression and hardware acceleration for neural networks: A comprehensive survey. *Proceedings of the IEEE*, 108(4):485–532, 2020.

[5] Song Han, Huizi Mao, and William J Dally. Deep compression: Compressing deep neural networks with pruning, trained quantization and huffman coding. *arXiv preprint arXiv:1510.00149*, 2015.

[6] Huan Wang, Suhas Lohit, Michael N Jones, and Yun Fu. What makes a" good" data augmentation in knowledge distillation-a statistical perspective. *Advances in Neural Information Processing Systems*, 35:13456–13469, 2022.

[7] Dohyung Kim, Junghyup Lee, and Bumsub Ham. Distance-aware quantization. In *Proceedings of the IEEE/CVF International Conference on Computer Vision*, pages 5271–5280, 2021.

[8] Yury Nahshan, Brian Chmiel, Chaim Baskin, Evgenii Zheltonozhskii, Ron Banner, Alex M Bronstein, and Avi Mendelson. Loss aware post-training quantization. *Machine Learning*, 110(11-12):3245–3262, 2021.

[9] Haoping Bai, Meng Cao, Ping Huang, and Jiulong Shan. Batchquant: Quantized-for-all architecture search with robust quantizer. *Advances in Neural Information Processing Systems*, 34:1074–1085, 2021.

[10] Sijie Zhao, Tao Yue, and Xuemei Hu. Distribution-aware adaptive multi-bit quantization. In *Proceedings of the IEEE/CVF Conference on Computer Vision and Pattern Recognition*, pages 9281–9290, 2021.

[11] Yongkweon Jeon, Chungman Lee, Eulrang Cho, and Yeonju Ro. Mr. biq: Post-training non-uniform quantization based on minimizing the reconstruction error. In *Proceedings of the IEEE/CVF Conference on Computer Vision and Pattern Recognition*, pages 12329–12338, 2022.

[12] Alex Finkelstein, Ella Fuchs, Idan Tal, Mark Grobman, Niv Vosco, and Eldad Meller. Qft: Post-training quantization via fast joint finetuning of all degrees of freedom. In *Computer Vision–ECCV 2022 Workshops: Tel Aviv, Israel, October 23–27, 2022, Proceedings, Part VII*, pages 115–129. Springer, 2023.

[13] Itay Hubara, Yury Nahshan, Yair Hanani, Ron Banner, and Daniel Soudry. Accurate post training quantization with small calibration sets. In *International Conference on Machine Learning*, pages 4466–4475. PMLR, 2021.

[14] Elias Frantar, Sidak Pal Singh, and Dan Alistarh. Optimal Brain Compression: a framework for accurate post-training quantization and pruning. *Advances in Neural Information Processing Systems*, 36, 2022.

[15] Markus Nagel, Rana Ali Amjad, Mart Van Baalen, Christos Louizos, and Tijmen Blankevoort. Up or down? adaptive rounding for post-training quantization. In *International Conference on Machine Learning*, pages 7197–7206. PMLR, 2020.

[16] Yuhang Li, Ruihao Gong, Xu Tan, Yang Yang, Peng Hu, Qi Zhang, Fengwei Yu, Wei Wang, and Shi Gu. Brecq: Pushing the limit of post-training quantization by block reconstruction. *arXiv preprint arXiv:2102.05426*, 2021.

[17] Markus Nagel, Marios Fournarakis, Rana Ali Amjad, Yelysei Bondarenko, Mart Van Baalen, and Tijmen Blankevoort. A white paper on neural network quantization. *arXiv preprint arXiv:2106.08295*, 2021.

[18] Raghuraman Krishnamoorthi. Quantizing deep convolutional networks for efficient inference: A whitepaper. *arXiv preprint arXiv:1806.08342*, 2018.

[19] Yunshan Zhong, Mingbao Lin, Mengzhao Chen, Ke Li, Yunhang Shen, Fei Chao, Yongjian Wu, and Rongrong Ji. Fine-grained data distribution alignment for post-training quantization. In *Computer Vision–ECCV 2022: 17th European Conference, Tel Aviv, Israel, October 23–27, 2022, Proceedings, Part XI*, pages 70–86. Springer, 2022.

[20] Xingchao Liu, Mao Ye, Dengyong Zhou, and Qiang Liu. Post-training quantization with multiple points: Mixed precision without mixed precision. In *Proceedings of the AAAI Conference on Artificial Intelligence*, volume 35, pages 8697–8705, 2021.

[21] Yaohui Cai, Zhewei Yao, Zhen Dong, Amir Gholami, Michael W Mahoney, and Kurt Keutzer. Zeroq: A novel zero shot quantization framework. In *Proceedings of the IEEE/CVF Conference on Computer Vision and Pattern Recognition*, pages 13169–13178, 2020.

[22] Markus Nagel, Mart van Baalen, Tijmen Blankevoort, and Max Welling. Data-free quantization through weight equalization and bias correction. In *Proceedings of the IEEE/CVF International Conference on Computer Vision*, pages 1325–1334, 2019.

[23] Edouard Yvinec, Arnaud Dapogny, Matthieu Cord, and Kevin Bailly. Spiq: Data-free per-channel static input quantization. In *Proceedings of the IEEE/CVF Winter Conference on Applications of Computer Vision*, pages 3869–3878, 2023.

[24] Xu Shoukai, Li Haokun, Zhuang Bohan, Liu Jing, Cao Jiezhang, Liang Chuangrun, and Tan Mingkui. Generative low-bitwidth data free quantization. In *The European Conference on Computer Vision*, pages 1–17. Springer, 2020.

[25] Yuang Liu, Wei Zhang, and Jun Wang. Zero-shot adversarial quantization. In *Proceedings of the IEEE/CVF Conference on Computer Vision and Pattern Recognition*, pages 1512–1521, 2021.

[26] Robert Geirhos, Patricia Rubisch, Claudio Michaelis, Matthias Bethge, Felix A Wichmann, and Wieland Brendel. Imagenet-trained cnns are biased towards texture; increasing shape bias improves accuracy and robustness. In *International Conference on Learning Representations*, 2019.

[27] Yingwei Li, Qihang Yu, Mingxing Tan, Jieru Mei, Peng Tang, Wei Shen, Alan Yuille, and Cihang Xie. Shape-texture debiased neural network training. *arXiv preprint arXiv:2010.05981*, 2020.

[28] Bo Gao and Michael W. Spratling. Shape-texture debiased training for robust template matching. *SENSORS*, 22(17), SEP 2022.

[29] Yunshan Zhong, Mingbao Lin, Gongrui Nan, Jianzhuang Liu, Baochang Zhang, Yonghong Tian, and Rongrong Ji. Intraq: Learning synthetic images with intra-class heterogeneity for zero-shot network quantization. In *Proceedings of the IEEE/CVF Conference on Computer Vision and Pattern Recognition*, pages 12339–12348, 2022.

[30] Xiangguo Zhang, Haotong Qin, Yifu Ding, Ruihao Gong, Qinghua Yan, Renshuai Tao, Yuhang Li, Fengwei Yu, and Xianglong Liu. Diversifying sample generation for accurate data-free quantization. In *Proceedings of the IEEE/CVF Conference on Computer Vision and Pattern Recognition*, pages 15658–15667, 2021.

[31] Laurens Van der Maaten and Geoffrey Hinton. Visualizing data using t-sne. *Journal of machine learning research*, 9(11), 2008.

[32] Zhenhua Guo, Lei Zhang, and David Zhang. A completed modeling of local binary pattern operator for texture classification. *IEEE transactions on image processing*, 19(6):1657–1663, 2010.

[33] Li Liu, Jie Chen, Paul Fieguth, Guoying Zhao, Rama Chellappa, and Matti Pietikäinen. From bow to cnn: Two decades of texture representation for texture classification. *International Journal of Computer Vision*, 127:74–109, 2019.

[34] Trygve Randen and John Hakon Husoy. Filtering for texture classification: A comparative study. *IEEE Transactions on pattern analysis and machine intelligence*, 21(4):291–310, 1999.

[35] Arden Sagiterry Setiawan, Julian Wesley, Yudy Purnama, et al. Mammogram classification using law's texture energy measure and neural networks. *Procedia Computer Science*, 59:92–97, 2015.

[36] Will D Gillett. Image classification using laws' texture energy measures. Technical report, Washington University in St. Louis, 1987.

[37] Yuwei Zhang, Peng Zhang, Chun Yuan, and Zhi Wang. Texture and shape biased two-stream networks for clothing classification and attribute recognition. In *Proceedings of the IEEE/CVF Conference on Computer Vision and Pattern Recognition*, pages 13538–13547, 2020.

[38] Taye Girma Debelee, Abrham Gebreselasie, Friedhelm Schwenker, Mohammadreza Amirian, and Dereje Yohannes. Classification of mammograms using texture and cnn based extracted features. *Journal of Biomimetics, Biomaterials and Biomedical Engineering*, 42:79–97, 2019.

[39] Leon Gatys, Alexander S Ecker, and Matthias Bethge. Texture synthesis using convolutional neural networks. *Advances in neural information processing systems*, 28, 2015.

[40] Pedro Ballester and Ricardo Araujo. On the performance of googlenet and alexnet applied to sketches. In *Proceedings of the AAAI conference on artificial intelligence*, volume 30, 2016.

[41] Robert Geirhos, Patricia Rubisch, Claudio Michaelis, Matthias Bethge, Felix A Wichmann, and Wieland Brendel. Imagenet-trained cnns are biased towards texture; increasing shape bias improves accuracy and robustness. *arXiv preprint arXiv:1811.12231*, 2018.

[42] Nikolai Kalischek, Rodrigo Caye Daudt, Torben Peters, Reinhard Furrer, Jan D Wegner, and Konrad Schindler. Biasbed-rigorous texture bias evaluation. In *Proceedings of the IEEE/CVF Conference on Computer Vision and Pattern Recognition*, pages 22221–22230, 2023.

[43] Cong Guo, Yuxian Qiu, Jingwen Leng, Xiaotian Gao, Chen Zhang, Yunxin Liu, Fan Yang, Yuhao Zhu, and Minyi Guo. Squant: On-the-fly data-free quantization via diagonal hessian approximation. *arXiv preprint arXiv:2202.07471*, 2022.

[44] Eldad Meller, Alexander Finkelstein, Uri Almog, and Mark Grobman. Same, same but different: Recovering neural network quantization error through weight factorization. In *International Conference on Machine Learning*, pages 4486–4495. PMLR, 2019.

[45] Yangcheng Gao, Zhao Zhang, Richang Hong, Haijun Zhang, Jicong Fan, and Shuicheng Yan. Towards feature distribution alignment and diversity enhancement for data-free quantization. In *2022 IEEE International Conference on Data Mining (ICDM)*, pages 141–150. IEEE, 2022.

[46] Biao Qian, Yang Wang, Richang Hong, and Meng Wang. Rethinking data-free quantization as a zero-sum game. *arXiv preprint arXiv:2302.09572*, 2023.

[47] Biao Qian, Yang Wang, Richang Hong, and Meng Wang. Adaptive data-free quantization. *arXiv e-prints*, pages arXiv–2303, 2023.

[48] Kanghyun Choi, Deokki Hong, Noseong Park, Youngsok Kim, and Jinho Lee. Qimera: Data-free quantization with synthetic boundary supporting samples. *Advances in Neural Information Processing Systems*, 34:14835–14847, 2021.

[49] Timo Ojala, Matti Pietikäinen, and David Harwood. A comparative study of texture measures with classification based on featured distributions. *Pattern recognition*, 29(1):51–59, 1996.

[50] Khurram Kamal, Rehan Qayyum, Senthan Mathavan, and Tayyab Zafar. Wood defects classification using laws texture energy measures and supervised learning approach. *Advanced Engineering Informatics*, 34:125–135, 2017.

[51] Hongyi Zhang, Moustapha Cisse, Yann N Dauphin, and David Lopez-Paz. mixup: Beyond empirical risk minimization. In *International Conference on Learning Representations*, 2018.

[52] Alex Krizhevsky, Geoffrey Hinton, et al. Learning multiple layers of features from tiny images. 2009.

[53] Olga Russakovsky, Jia Deng, Hao Su, Jonathan Krause, Sanjeev Satheesh, Sean Ma, Zhiheng Huang, Andrej Karpathy, Aditya Khosla, Michael Bernstein, et al. Imagenet large scale visual recognition challenge. *International journal of computer vision*, 115:211–252, 2015.

[54] Kaiming He, Xiangyu Zhang, Shaoqing Ren, and Jian Sun. Deep residual learning for image recognition. In *Proceedings of the IEEE conference on computer vision and pattern recognition*, pages 770–778, 2016.

[55] Mark Sandler, Andrew Howard, Menglong Zhu, Andrey Zhmoginov, and Liang-Chieh Chen. Mobilenetv2: Inverted residuals and linear bottlenecks. In *Proceedings of the IEEE conference on computer vision and pattern recognition*, pages 4510–4520, 2018.

[56] Adam Paszke, Sam Gross, Francisco Massa, Adam Lerer, James Bradbury, Gregory Chanan, Trevor Killeen, Zeming Lin, Natalia Gimelshein, Luca Antiga, et al. Pytorch: An imperative style, high-performance deep learning library. *Advances in neural information processing systems*, 32, 2019.

[57] Ilya Loshchilov and Frank Hutter. Sgdr: Stochastic gradient descent with warm restarts. In *International Conference on Learning Representations*, 2016.

[58] Baozhou Zhu, Peter Hofstee, Johan Peltenburg, Jinho Lee, and Zaid Alars. Autorecon: Neural architecture search-based reconstruction for data-free. In *International Joint Conference on Artificial Intelligence*, 2021.

[59] Kanghyun Choi, Hye Yoon Lee, Deokki Hong, Joonsang Yu, Noseong Park, Youngsok Kim, and Jinho Lee. It's all in the teacher: Zero-shot quantization brought closer to the teacher. In *Proceedings of the IEEE/CVF Conference on Computer Vision and Pattern Recognition*, pages 8311–8321, 2022.